# Phase–Property Diagrams for Multicomponent Oxide Systems toward Materials Libraries

*Leonardo Velasco,\* Juan S. Castillo, Mohana V. Kante, Jhon J. Olaya, Pascal Friederich, and Horst Hahn*

Exploring the vast compositional space offered by multicomponent systems or high entropy materials using the traditional route of materials discovery, one experiment at a time, is prohibitive in terms of cost and required time. Consequently, the development of high-throughput experimental methods, aided by machine learning and theoretical predictions will facilitate the search for multicomponent materials in their compositional variety. In this study, high entropy oxides are fabricated and characterized using automated high-throughput techniques. For intuitive visualization, a graphical phase–property diagram correlating the crystal structure, the chemical composition, and the band gap are introduced. Interpretable machine learning models are trained for automated data analysis and to speed up data comprehension. The establishment of materials libraries of multicomponent systems correlated with their properties (as in the present work), together with machine learning-based data analysis and theoretical approaches are opening pathways toward virtual development of novel materials for both functional and structural applications.

## 1. Introduction

Studies and development of doped oxides or metallic alloys require extensive experimental efforts. The chemical space of the investigated materials increases as more elements are added or exchanged. Additionally, by varying even one experimental parameter (e.g., an extra heat treatment during sample fabrication) will require an extra characterization for each of the produced samples, leading to more data points to be collected and interpreted. In the upcoming era of information- and design-oriented material discoveries, the time-consuming traditional methodologies (one experiment at a time) for synthesis and characterization are being complemented by high-throughput (HT) technologies. Consequently, for material systems, such as thin films and materials, with their many possible combinations in the compositional space along with their rich suite of processing parameters, HT technologies (for their synthesis and characterization) are being presently developed and integrated with machine learning techniques.[1–3] Furthermore, the transition toward higher compositional complexity, combined with the enormous amount of combinatorial possibilities has contributed to the development of high entropy materials (HEMs).[4–6] HEMs are single-phase multicomponent (five or more elements) metallic or ceramic systems with near-equiatomic concentrations.[6] Hence, investigating the HEMs by using traditional procedures of material discoveries becomes impractical mostly because they require a high number of experimental efforts and complex data analysis and interpretation.

In addition to the chemical complexity of HEMs, the synthesis, description, and visualization of phases and their underlying properties are in per se challenging and thus necessitating the development of new concepts to aid in identifying the key microstructural components and quantifying their properties. The family of HEMs encompasses high entropy alloys, carbides, nitrides, borides, sulfides, and oxides.[7–9] Their promising structural and functional properties with potential applications in batteries,[10] cutting tools and hard coatings,[6] solar absorber coatings, and diffusion barrier films,[11] have triggered widespread interest in a number of research groups around the world. HEMs, constituted of several majority elements, are placed in the center of multicomponent phase

L. Velasco, J. S. Castillo, M. V. Kante, P. Friederich, H. Hahn
Institute of Nanotechnology
Karlsruhe Institute of Technology
Hermann-von-Helmholtz-Platz 1
76344 Eggenstein-Leopoldshafen, Germany
E-mail: leonardo.estrada@kit.edu

J. S. Castillo, J. J. Olaya
Facultad de Ingeniería
Universidad Nacional de Colombia
Av. Cra. 30 # 45-03, Ed. 407, Ciudad Universitaria
Bogotá, DC 111321, Colombia

J. S. Castillo, M. V. Kante, H. Hahn
Joint Research Laboratory Nanomaterials
Technische Universität Darmstadt
Otto-Berndt-Str. 3, 64206 Darmstadt, Germany

P. Friederich
Institute of Theoretical Informatics
Karlsruhe Institute of Technology
Am Fasanengarten 5, 76131 Karlsruhe, Germany

ⓘ The ORCID identification number(s) for the author(s) of this article can be found under https://doi.org/10.1002/adma.202102301.

ADVANCED
SCIENCE NEWS
www.advancedsciencenews.com

ADVANCED
MATERIALS
www.advmat.de

diagrams. Hence, the vast compositional space enabling a variety of atomic structures, phases, and properties needs to be explored. The challenge, even without considering additional parameters offered by the microstructural design, such as grain size and defect density, is enormous and requires new approaches of material development, which are based on HT experiments and the formulation of intensive data analysis concepts.[3,12–20]

HT methods integrated with machine learning techniques have been used for the fabrication of organic–inorganic perovskites,[15,21–24] carbon nanotubes,[20,25–28] organic materials,[29–33] multicomponent materials up to four components,[2,19,34–55] and multicomponent materials (i.e., HEMs or >5 elements).[1,51,54–59] The aforementioned HT methods combined with machine learning are paving the way to the formulation of autonomous protocols for materials discovery. Thus far, however, the aforementioned research efforts are limited, principally due to the automation flexibility. For example, automated synthesis of organic materials (using automated pipetting robots) seems to be more straightforward compared to metallic alloys (produced by physical vapor deposition, additive manufacturing, and other traditional synthesis techniques). In materials science, one of the most common but time-consuming method to investigate the crystal structure of a material is X-ray diffraction (XRD).[60] Even though XRD is a very useful and irreplaceable method for characterizing the crystal structure that can in turn directly correlate to the properties of the material,[61] the interpretation of X-ray diffractograms requires a unique set of experience and expertise and it is also time consuming (e.g., peak indexing, space group determination, lattice parameter). In some cases, the analysis of the X-ray data requires the use of specific software packages (as, e.g., "Jade" computer software) to extract the proper crystal structure parameters. Presently, efforts are underway to employ automated XRD data gathering and automated data analysis combined with the use of machine learning to speed up computation of crystal structure parameters and their subsequent correlations to corresponding material properties. The use of these two automated sequential approaches in combination with machine learning has greatly speed up the formulation of structure–properties correlations with recent studies showing that automation and machine learning have yielded satisfactory results.[60–65]

Depending on the synthesis or characterization method applied to a family of materials for a specific field of applications, the amount of time needed to produce or characterize a single material can vary from few minutes to several hours or even days. In the specific case of the HEMs family, in addition to their chemical complexity, the automation flexibility seems to be one of the major bottlenecks, specifically with regard to the evaluation of the crystal structure and relevant properties that are necessary to be considered (e.g., crystal structure, chemical composition, and functional properties).[55,60] The use of traditional synthesis, processing, and characterization techniques when applied to one sample at a time will unavoidably result in the vast chemical complexity combinations of the HEMs to be largely unaddressed and thus creating a knowledge gap that in turn negatively impacts the gaining of fundamental understanding of the structure and properties that these very interesting and novel materials can have.

The visualization of multicomponent materials (five or more elements), as described in the critical review of high entropy alloys by Miracle and Senkov, requires the ability to visualize high-dimensional composition space.[66] Integration of properties into a phase diagram has been successfully achieved for ternary systems (2D representation) and up to some extend for quaternary systems (3D tetrahedron or its 2D cutting planes).[66] The complexity of the compositional space visualization increases with the number of different elements and their corresponding amounts present in the material. Nevertheless, even for the case of a 5-components system useful representations have been developed.[66–70] Each visualization type has both advantages and disadvantages and depending on the aim of the study (as, e.g., with regard to the relevant information space to be shown), each type of visualization can be useful in its own way. For instance, by using isopleth diagrams it is possible to represent the effect of composition and temperature on the crystal structure of a multicomponent quinary system,[69] although the ~~effect of composition and temperature~~ variations on the structure is limited to the changes introduce by only one element. In the present study, a visual representation of the compositional space around an equiatomic multicomponent system will be displayed for the case of compositionally complex near-equiatomic oxides (these materials are often referred as high entropy oxides [HEOs]). The visualization of information on the crystal structure, the chemical composition, and a functional property in a 2D diagram will aid the exploration and the study of this class of materials.

One of the HEMs that has received a lot of attention are the HEOs. These multicomponent ceramics, for the first time described in 2015, have since shown potential for functional applications in electrodes for next-generation Li-ion batteries,[10] band gap engineering,[71] and catalysts.[72] Therefore, exploring different HEO systems and their vast compositional space can lead to the discovery of materials with novel compositions and properties, and their potential use in technological applications. HEOs can be synthesized using several methods, among which are methods based on solid state reaction or wet chemistry.[8,73,74] To power further combinatorial studies and encourage theoretical advancements, we developed a HT synthesis method to explore a significant number of HEOs. Our HT methodology, based on reverse co-precipitation[73] and using water-soluble precursors, was used to establish a materials library, here illustrated by the example of a rare earth-based HEO system $(Ce_{0.2}Pr_{0.2}La_{0.2}Sm_{0.2}Y_{0.2})O_{2-\delta}$. A total number of 106 compositions were fabricated and characterized by XRD, Raman spectroscopy, chemical composition analysis, and ultraviolet–visible (UV–vis) spectroscopy, all the techniques are automated and expandable for a much larger number of samples. The synthesis was conducted using an automated pipetting system, similar to pioneering studies in other fields of materials research.[1,15,24,41,75] The XRD characterization platform is connected to machine learning enhanced data analysis method. Following a methodology proposed in similar studies,[1,3,17,19,21,23,24] the results from the data analysis can be used to build materials libraries, as it is displayed in the work flow diagram in **Figure 1**. Further automation and integration of artificial intelligence[20,76–78] will enable the use of a closed-loop platform for autonomous exploration of
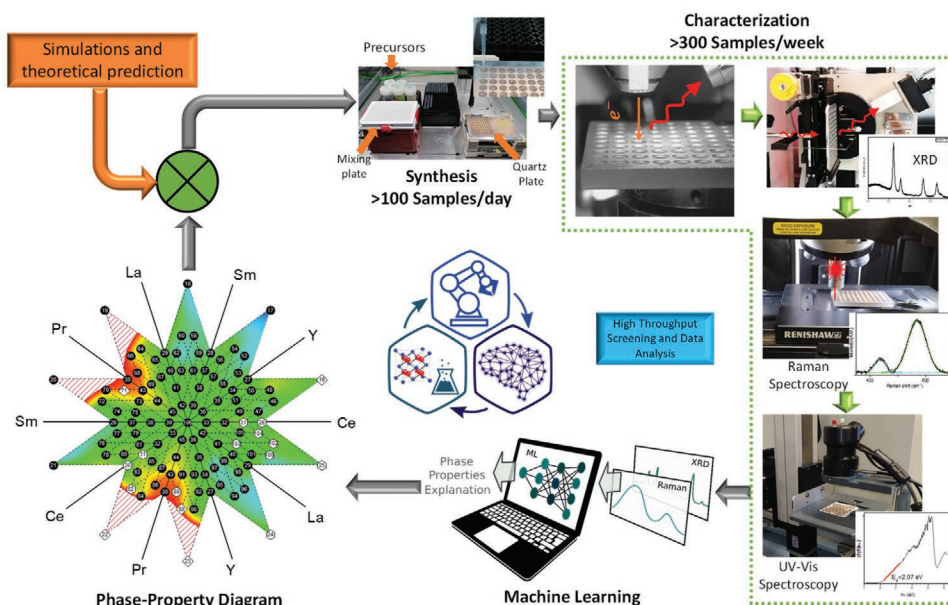
**2102301** (2 of 11)

**Figure 1.** Work flow diagram for the development of phase–property diagrams and materials libraries. Automated synthesis and characterization integrated with machine learning speeds up data comprehension, and the visualization of the multicomponent phase–property (band gap) diagram (materials library). The loop is closed by determining the best candidates for a desired property, or by narrowing specific regions of interest to initiate further studies. Multicomponent materials that are theoretically predicted can be used as an external input to the automated loop.

high-dimensional phase spaces and efficient optimization of material properties.[3,12–20]

## 2. Main

The following 106 oxide compositions, based on the five cations in $(Ce_{0.2}Pr_{0.2}La_{0.2}Sm_{0.2}Y_{0.2})O_{2-\delta}$ HEO, were fabricated using the automated pipetting system (see experimental section for a detailed description): individual-single cation (5 samples), binary equiatomic (10 combinations), ternary equiatomic (10 combinations), quaternary equiatomic (5 combinations), quinary non-equiatomic compositions (75 combinations), and the equiatomic HEO $(Ce_{0.2}Pr_{0.2}La_{0.2}Sm_{0.2}Y_{0.2})O_{2-\delta}$ (1 sample). The 106 samples were characterized following the work flow presented in Figure 1. See experimental section for a detailed description and Section S10, Supporting Information, for each sample X-ray diffractogram; percentage of phases, crystallite sizes, lattice parameters, and chemical compositions in Table S1, Supporting Information; and chemical composition map in Figures S1 and S2, Supporting Information.

In **Figure 2**, an isothermal phase diagram for the single cation and binary cation oxides is presented. The structural data are plotted as a function of composition with the value for 100 at.% in the center. For example, the pure (single cation) $Y_2O_3$ oxide is represented by the hexagon #1 (with the hexagon symbol indicating the Ia-3 structure) and it is placed in the plot at an angle of 54° and 162° (measured from the top in the clockwise direction). Similarly, the other pure oxides are plotted with their respective structures, full circles and full squares for Fm-3m and P63/m, respectively. The binary equiatomic oxides are plotted between their respective pure oxides at the 50 at.% position. For example, the open diamond marker (sample #7)

indicates a 50/50 binary of La and Sm oxide, which exhibits a multiple phase structure, while the full circle (sample #14) indicates a single-phase Fm-3m structure for a 50/50 binary of Sm and Ce oxide. Figure 2 shows that the single oxides and the binary oxides without La display a single-phase crystal structure (Fm-3m, Ia-3, or P63/m). The presence of multiple phases in the binary oxides containing La can be attributed to several factors such as annealing temperature, tendency to form a solid solution, and the oxidation state of the elements.[79]

A more complex multicomponent phase diagram with up to five cations is displayed in **Figure 3** for all the samples containing three or more elements (total of 91 samples). The position of each data point in Figure 3a is related to the chemical composition of the corresponding sample, the symbols are used to note if the specific composition has multiple phases or not, while the contour color map represents the configurational entropy ($S_{config}$) for each of the 91 samples, calculated using Equation (1).

$$S_{config} = -R\left[X\left(\sum_{M}^{a=1} X_a ln X_a\right)\right] \tag{1}$$

where $X_a$ is the mole fraction of the cation site constituent element (i.e., Ce, La, Sm, Pr and Y), and $M$ is the number of cations. For simplicity, the contribution to $S_{config}$ from the anion site ($O^{2-}$) is assumed to be zero.

Each of the axis in Figure 3a represents the addition of a cation to an equiatomic quaternary system (from 0 to 20 at.% in intervals of 5 at.%). For instance, the Ce axis represents the addition of Ce to the quaternary system $(Ce_xPr_{(1-x)/4}La_{(1-x)/4}Sm_{(1-x)/4}Y_{(1-x)/4})O_{2-\delta}$, that is, the outer point in the Ce axis is equivalent to add 0 at.% Ce (sample #26 $(Pr_{0.25}La_{0.25}Sm_{0.25}Y_{0.25})O_{2-\delta}$); the first inner point

○ Single Phase $Ia\bar{3}$   ● Single Phase $Fm\bar{3}m$   ■ Single phase $P63/m$   ◇ Multiple Phase
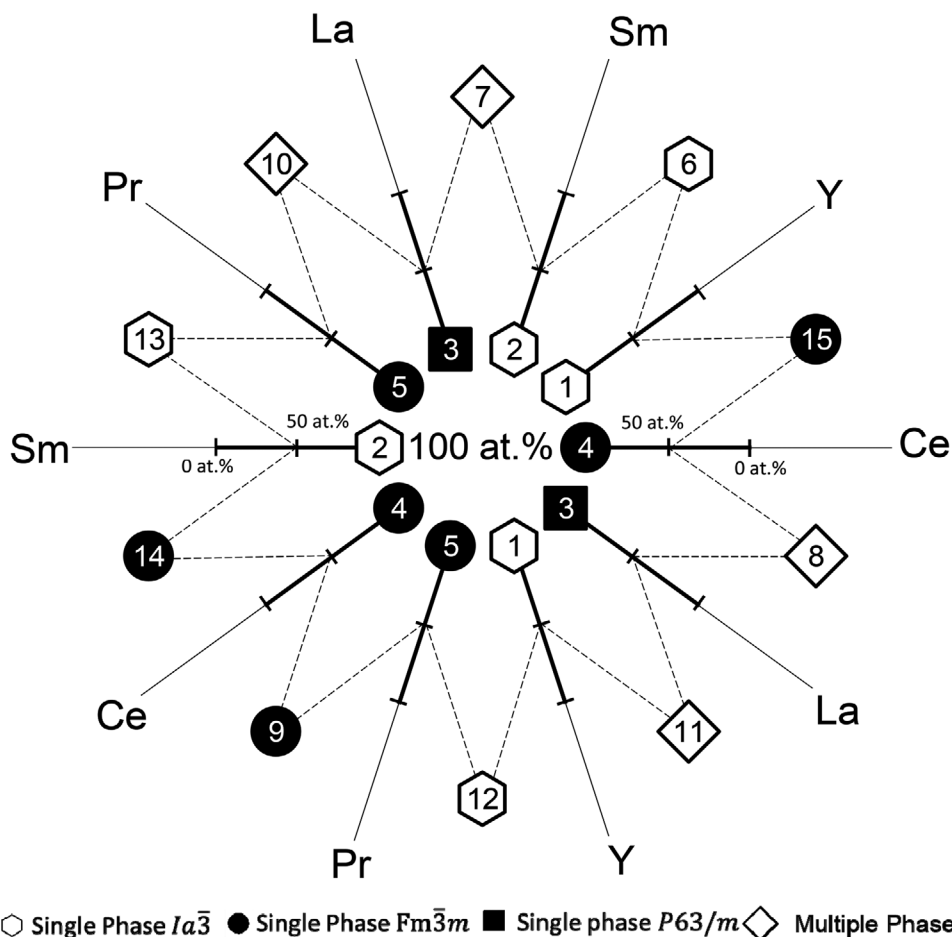
**Figure 2.** Isothermal phase diagram at 750 °C for single and binary oxides (samples #1–15), notice that the axis representing the single cation oxides are repeated to facilitate the binary oxides visualization. The symbols at the respective compositions show the single or multiple phase nature of the samples (see X-ray diffractograms in Section S10, Supporting Information). Details on how to read/interpret Figure 2 are discussed in the text.

in the Ce axis is equivalent to add 5 at.% Ce (sample #31 $(Ce_{0.05}Pr_{0.237}La_{0.237}Sm_{0.237}Y_{0.237})O_{2-\delta}$); the second inner point in the Ce axis is equivalent to add 10 at.% Ce (sample #32 $(Ce_{0.1}Pr_{0.225}La_{0.225}Sm_{0.225}Y_{0.225})O_{2-\delta}$); the third inner point in the Ce axis is equivalent to add 15 at.% Ce (sample #33 $(Ce_{0.15}Pr_{0.212}La_{0.212}Sm_{0.212}Y_{0.212})O_{2-\delta}$); and the center of the phase diagram is equivalent to add 20 at.% Ce (sample #106 $(Ce_{0.2}Pr_{0.2}La_{0.2}Sm_{0.2}Y_{0.2})O_{2-\delta}$). The points between two axes represent the process of adding two cations to an equiatomic ternary system. For example, the points between Ce and Y axes (samples #46–51) represent the addition of Ce and Y to the system $(Ce_xY_zLa_{(1-x-z)/3}Sm_{(1-x-z)/3}Pr_{(1-x-z)/3})O_{2-\delta}$. The composition of samples #46 to 51 can be obtained as described for sample #48 and #51: the dashed lines parallel to the Ce and Y axis lead to the concentration of Ce and Y in the respective sample. Thus sample #48 contains 10 at.% Ce and 5 at.% Y, resulting in an overall composition $(Ce_{0.1}Y_{0.05}La_{0.283}Sm_{0.283}Pr_{0.283})O_{2-\delta}$. Sample #51 contains 15 at.% Ce and 10 at.% Y, resulting in an overall composition $(Ce_{0.15}Y_{0.1}La_{0.25}Sm_{0.25}Pr_{0.25})O_{2-\delta}$. The outer intersection of the two axes (outer corner tip of the plot), is the ternary system containing 0 at.% Ce and 0 at.% Y $(La_{0.33}Sm_{0.33}Pr_{0.33})O_{2-\delta}$ (sample #16). Among the 91 samples displayed in Figure 3a, 76 samples crystallized in a single

fluorite phase (Fm-3m), 10 samples crystallized in a single bixbyte phase (Ia-3), and 5 samples showed the presence of multiple phases. A crystallographic map of the investigated samples is presented in Figure 3b, which allows to visualize that the majority of the quinary systems tend to crystallize in a fluorite structure.

One interesting result is that some of the systems without Ce also formed a single phase, except for the ternary systems $(La_{0.33}Sm_{0.33}Y_{0.33})O_{2-\delta}$ (sample #22) and $(Pr_{0.33}Sm_{0.33}La_{0.33})O_{2-\delta}$ (sample #16). By contrast, a previous study has concluded that Ce can play a significant role in stabilizing a single-phase crystal structure in a multicomponent system, whereas the absence of Ce leads to the formation of multiple phases.[71] Therefore, samples (systems that do not contain Ce,) #21, #25, and #26 were repeated using the automated pipetting system. Additionally, sample #26 was manually synthesized using reverse co-precipitation. The X-ray diffractograms (Figure S3, Supporting Information for samples #21, #25, and #26) and further analysis of sample #26 using transmission electron microscopy (Figure S4, Supporting Information) confirmed that the samples crystallized in a single phase. The HT screening results suggest that Ce, being $^{+4}$, and Pr, being mixed state $^{+3}$ or $^{+4}$, can stabilize a single-phase structure. The strong influence of

**ADVANCED
SCIENCE NEWS**

www.advancedsciencenews.com
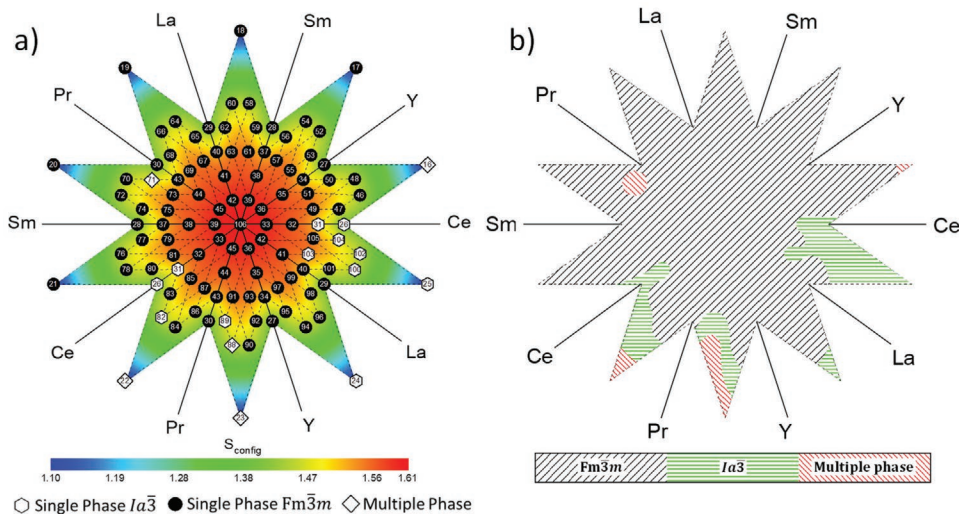
**ADVANCED
MATERIALS**

www.advmat.de

**Figure 3.** Isothermal phase diagrams at 750 °C for 91 oxides, highlighting which of the oxides yields a single or a multiple phase. a) Isothermal multi-component phase diagram at 750 °C comprising 91 compositions for the chemical deviations from the HEO system $(Ce_{0.2}Pr_{0.2}La_{0.2}Sm_{0.2}Y_{0.2})O_{2-\delta}$ (samples #16–106, containing three or more elements). The symbols at the respective compositions show the single or multiple phase nature of the samples (see X-ray diffractograms in Section S10, Supporting Information). The contour color map relates the configurational entropy $S_{config}$ for each of the samples, calculated using Equation (1). b) Isothermal crystallographic phase map obtained for the chemical space of 91 oxides. Note that in order to fit all the 91 samples in one multicomponent phase diagram the constituent cation axes are repeated, and therefore the amount of points in the figure increases by 20. Details on how to read/interpret Figure 3 are discussed in the text.

Ce and/or Pr cations in stabilizing a single phase becomes evident as the entropy decreases, that is, even systems with lower entropy could be stabilized in a single phase as long as a $^{+4}$ or mixed $^{+3,+4}$ cation is present. Among the five samples that displayed multiple phases, four showed a small amount (<2%) of secondary phase, perhaps longer times or higher temperatures during the heat treatment may have resulted in further reduction of the second phase content or even complete single-phase formation. For the system $(La_{0.33}Sm_{0.33}Y_{0.33})O_{2-\delta}$ (sample #22), several phases were encountered, in this case, similar to the explanation given above, there is no $^{+4}$ cation or mixed valence cation ($^{+3,+4}$) present.

One of the bottlenecks toward a fully autonomous and faster synthesis and characterization platform of multicomponent systems is the data analysis, in our case for the XRD data,[60] which to-date can require manual steps to analyze diffractograms and to determine the underlying crystal structure(s). To speed up the data analysis, we developed an adaptable and highly interpretable machine learning approach. This approach is capable of determining, in a shorter amount of time, whether an X-ray diffractogram is representative of a pure single phase or whether there are multiple phases present in a sample and thus providing intuitive explanations for the prediction (further details are provided in the experimental section). An example of the predictive power of the approach is illustrated for the multi-phase sample $(Sm_{0.5}Y_{0.5})O_{2-\delta}$, along with an explanation why the ML models classifies it as multi-phase, as shown in **Figure 4**a (further examples in Section 5, Supporting Information). A second machine learning model, trained directly on the materials compositions in the experimental dataset, was used to obtain feature importance values that are interpretable as well. While supporting the hypothesis that the simultaneous presence of both Ce and/or Pr stabilizes a single-phase material

(Figure 4b), the analysis furthermore shows that Y and Pr exert an even stronger stabilizing influence (Figure 4c), while high concentrations of Sm and La correlate with mixed phases systems (Figure 4d).

The search for compositionally complex materials, such as HEOs, is driven by the potential to identify as yet undiscovered scientifically interesting and technological relevant materials with unique novel properties for future applications. Typically, a functional material contains a well-balanced combination of major elements and dopants. For example, ceria doped with other rare earth elements or the addition of Ce to multicomponent oxides has resulted in materials that are used for UV light blockers, gas sensors, oxygen separation membranes, oxygen storage capacitors, catalysts, and solid oxide fuel cells. All these material applications depend on the absence of stoichiometry, originating from oxygen vacancy concentration[80] (OVC). Additionally, engineering the band gap (BG) of rare earth oxides, like in $CeO_2$, opened the possibility to make the material photoactive in the visible light spectrum with its potential use in photocatalytic applications.[81–83] It is well known that Raman spectroscopy is a powerful tool to compare OVC in rare earth metal oxides with a fluorite structure, which can be achieved by finding the ratio between the intensities of the peaks at ≈560–600 and ≈460 cm$^{-1}$ ($I_{560}/I_{460}$) in the Raman spectra.[84] Out of the 91 compositions presented in Figure 3, 76 samples show a single-phase fluorite structure, while in 3 samples the fluorite structure is nearly 98%, that is, a total of 79 samples can be considered to possess a fluorite structure. Meanwhile, the BG of oxides can be obtained from UV–vis spectroscopy.

As an example of the potential use of the phase–property diagram concept developed in the present study, the OVC and BG were measured and combined with the structural information. Further details for the OVC and BG calculation using
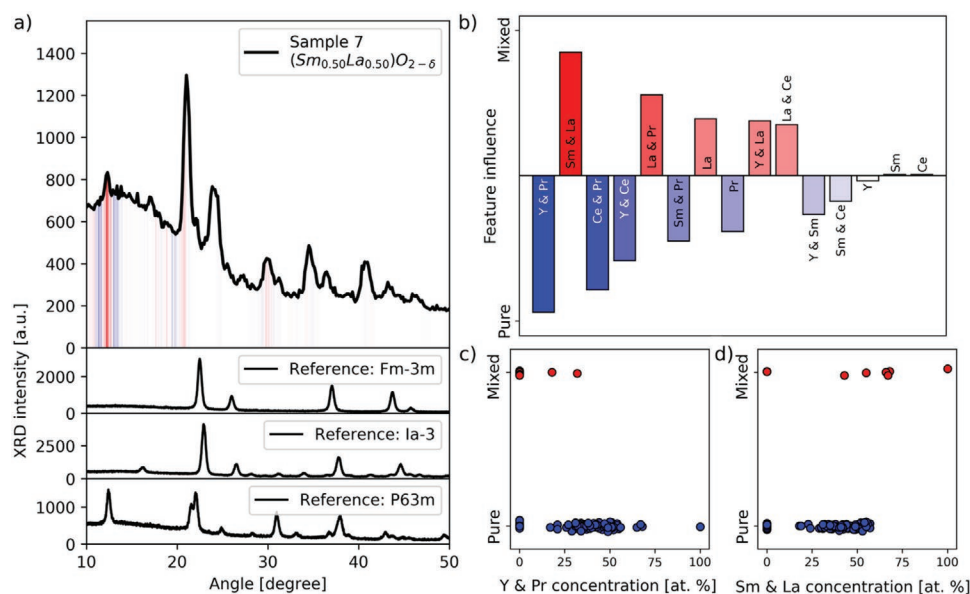
**Figure 4.** Machine learning models. a) Example of a correct ML prediction of a mixed phase XRD measurement, including explanations (red: toward mixed phase, blue: toward pure phase). b) Feature influences computed using a logistic regression model. c,d) Most relevant composition features used by the logistic regression model to predict pure and mixed phases.

automated Raman spectroscopy and automated UV–vis spectroscopy, respectively, are given in the experimental section. **Figure 5**a shows the landscape of OVC integrated with the structural data from Figure 3. The OVC was also empirically estimated and it is plotted in Figure S7, Supporting Information. Only small differences can be observed between the landscapes of experimental and calculated OVC, which can be attributed to the accuracy of the measurement. In Figure 5a, red regions have the highest OVC value, while dark blue regions have the lowest OVC value. Although OVC cannot be considered as a

property of the material, it is possible to conclude that compositions in the red and yellow regions in Figure 5a are possible candidate materials for solid oxide full cells.[80] Meanwhile, the green and blue regions in Figure 5a can be chosen for applications requiring low OVC.

Figure 5b shows the landscape of the direct BG (samples #16–106) integrated with the structural data from Figure 3. The BG values for all the samples can be found in Table S2, Supporting Information, along with the references of BGs reported in literature for some of the same systems as ours (it is worth
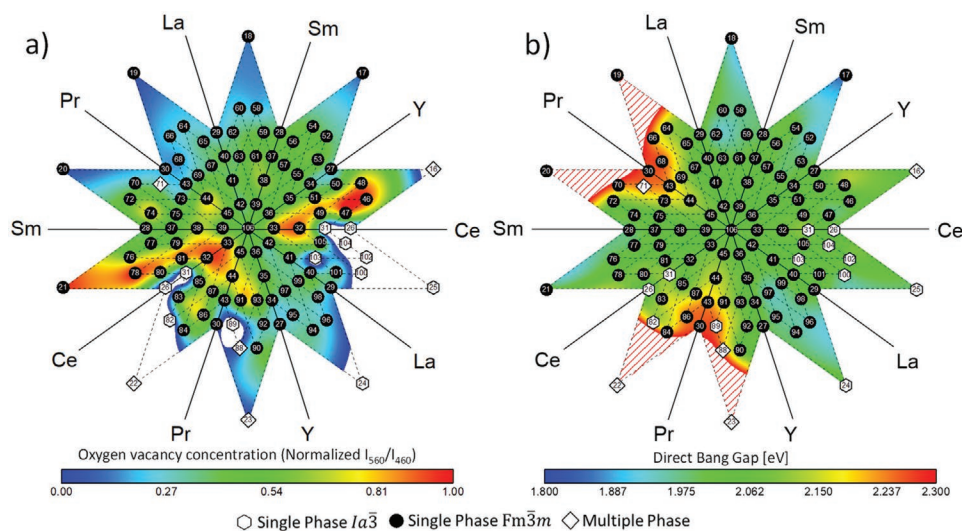


**Figure 5.** Landscape for the oxygen vacancy concentration ($I_{560}/I_{460}$) and the direct band gap in the isothermal multicomponent phase–property diagram at 750 °C. a) The contour color map visualizes the landscape of OVC obtained by the comparison of the $I_{560}/I_{460}$ ratio for each sample. The blank sections in the contour plot belong to samples that have an Ia-3 crystal structure or multiple phase structures. b) The contour color map shows the direct band gap obtained for each sample. The band gap value for samples 19, 20, 22, and 23 is >3 eV (see text and Table S2, Supporting Information for the band gap values of all the samples) and to enhanced visualization, the relevant area was shaded with red lines. The symbols are used to highlight if the specific sample displays or not multiple phase (refer to Figure 3 section for a detailed explanation on the figure interpretation).

**ADVANCED
SCIENCE NEWS**

www.advancedsciencenews.com

**ADVANCED
MATERIALS**

www.advmat.de

noting that only 18 BGs, out of the 106 samples produced in this study, have been reported in the literature). Figure 5b can be divide in three regions according to the variation of the BG. The regions with red color (BG range within 2.17–2.26 eV) belong to samples with low Pr content (between the axes labeled with Pr-Ce, Pr-La, Pr-Sm, and Pr-Y). An intermediate green colored region within the midrange of the BG values (BG range within 1.98–2.17 eV) contains samples with low Ce content (between the axes labeled with Ce-La, Ce-Sm, and Ce-Y). The lower BG values are in the blue regions (BG range within 1.86–1.98 eV) and emerged for the samples with high amounts of both Ce and Pr (between the axes labeled with La-Sm, La-Y, Sm-Y). The energy difference between the energy levels of Pr 4f and O 2p is the lowest ($\approx1.9$ eV) among the cations used in the present study, which results in low BGs (as low as $\approx1.9$ eV) in Pr containing systems.[71,85,86] Hence, samples without or low Pr content are expected to display higher BGs. Similarly, the energy difference between Ce 4f and O 2p is $\approx3.2$ eV, which is lower compared to that of La4f/Sm4f/Y5d and O 2p ($\approx5.5$eV) and still greater than the energy difference between Pr 4f and O 2p.[86] Therefore, high contents of both Ce and Pr contribute to a low BG values, and samples with low amounts of Ce and high amounts of Pr contribute to an intermediate BG values. The BG value follows a trend according to the concentration of the cations $\underset{Ce\uparrow Pr\uparrow < Ce\downarrow Pr\uparrow < Pr\downarrow}{1.86eV < 2eV < 2.2eV}$. It is noteworthy that the BG value changes in the contour plot from the center to the corners and it depends on the variation of Pr and Ce content.

Depending on the desired functional property or the intended application, such phase–property diagrams, here with the integrated BG landscape, allows the selection of the most promising candidates. Figure 5 can be considered as the starting point for selecting a multicomponent material with a desired functional property and subsequent refinement by narrowing the compositional variations. For example, if a multicomponent material with a single-phase fluorite structure that has a high amount of OVC and a low BG value is desired then the optimum candidates (based on Figure 5) could be samples 32, 46, 48, 78, and 81. The aforementioned example of a material with a single-phase structure, illustrates the possibility of employing the power of the phase–property diagram for selecting a single-phase material, among many different combinations of elements, crystallographic structures, or functional properties.

## 3. Conclusion

The systematic elaboration of phase–property diagrams for multicomponent systems will eventually lead to an understanding of the crystal structure evolution and of the stabilizing factors in these materials. Moreover, by integrating the measured property values into the phase diagram, the optimum chemical composition for a desired set of properties can be identified or at least the compositional region of interest can be narrowed down, hence, facilitating the search for the composition that likely yields the desired set of properties for the intended functional application. However, the proposed phase–property diagram visualization is only one possibility among other options to visualize materials libraries.[66–70]

The HT screening of many different chemical variations of the 5-cation HEO system made it possible to show that not only Ce but also Pr can stabilize multicomponent rare earth oxides in a single-phase crystal structure. In this study, at least 78 of the produced samples have not been reported before in the literature (see Table S2, Supporting Information), even 2 ternaries were not reported (possibly because they do not form single-phase crystalline structures).

The range of possibilities for the present methodology are far reaching. For example, in the present study, the BG value varied from $\approx1.86$ to $\approx2.26$ eV within the quinary systems (all the samples were calcined at the same temperature, i.e., an isothermal phase diagram). It has been shown that the BG of the HEO chosen for the present proof of principle study can be further tuned from $\approx2$ eV up to $\approx3.21$ eV[86] upon heat treatment in a reducing atmosphere. Furthermore, by performing heat treatments at higher or lower temperatures it will be possible to further vary the BG values. Certainly, further studies should be conducted using the automated methodologies, leading to comprehensive microstructure–property relationships.

The currently available robotic system can fabricate more than 100 samples per day, while the automated characterization of structure and properties for 300 samples typically requires 1 week. Thus, in 1 year, with only one set of fairly inexpensive HT equipment and without further optimization, it is possible to synthesize and characterize more than 15 000 combinations, which allows to establish the complex structure–property relationships even for very complex multicomponent materials. Automated and potentially machine learning enhanced data analysis, as shown here for the example of XRD diffractograms, paves the way to a fully automated and autonomous HT screening platform. By combining such automated platform with AI models,[3,18] it will be possible to achieve a high degree of autonomy for the efficient exploration of large materials parameter spaces and thus increasing the likelihood for new materials discovery. Conducting experimental combinatorial studies from all the combinations of elements in the periodic table, one experiment at a time, is an intractable task. Instead, our study aims to encourage further development of theoretical and simulation approaches in the field of multicomponent systems to provide targeted compositions that can be explored using HT methods. This synergistic approach should have the dual benefits of shorting the time for new materials discovery and increasing its likelihood.

Although HT has been used for decades, only now it is implemented in the field of ceramic multicomponent oxide materials (at least five elements). In our study we have demonstrated that by using an automated synthesis approach (based on liquid precursors metal salts), in analogous to HT studies in organic chemistry, it is possible to produce ceramic materials and implement doping studies. As many ceramics can be fabricated using wet chemistry methods, like reverse co-precipitation, it is possible to extrapolate our synthesis fabrication to not only fabricate multicomponent oxides but also multicomponent metal carbides, metal nitrides, metal sulfides, metal oxynitrides, among many other types of ceramic materials. It is important to highlight that the automated wet chemistry method can be further developed into a highly autonomous fashion, such that several parameters of the synthesis process (e.g., solution

concentration, precipitating agent and precursor solution ratio, and drying temperatures) can be monitored toward optimized experimental conditions.

## 4. Experimental Section

*Automated Sample Synthesis—From Nitrate Salts to Oxides*: The nitrate salts of Ce, La, Pr, Sm, and Y were used as precursors, and a water-based solution for each of the salts with a concentration of $0.1 \, \text{mol L}^{-1}$ was prepared and stirred for 1 h.

Nitrate salts:

$Ce(NO_3)_3 \cdot 6H_2O$, ALFA AESAR, 99.9%
$La(NO_3)_3 \cdot 6H_2O$, Sigma-Aldrich, 99.9%
$Pr(NO_3)_3 \cdot 6H_2O$, ABCR, 99.9%
$Sm(NO_3)_3 \cdot 6H_2O$, ABCR, 99.9%;
$Y(NO_3)_3 \cdot 6H_2O$, ABCR, 99.9%

The automated combination of the water-based solutions was achieved by using a pipetting robot (opentrons OT-2) and the entire process is described as follows:

**Step 1**: The water-based nitrate salts solutions, in desired volumes (in Table S1, Supporting Information, the amount of volume that was used for each mix is presented) are transferred and combined in a designated well position of a standard 360 µL 96-well plate. The solutions in the standard plate are mixed and stirred during the whole process. The formation of the desired oxides requires high temperatures (>700 °C) and the standard plate (made of polymer) is not suitable for such temperatures. Therefore, quartz plates ($70 \times 60 \times 5$ mm, with 0.3 mm well deepening and 5 mm diameter per well, total of 99 wells) were fabricated and are used for the high temperature oxide formation process.

**Step 2**: To initiate the reverse co-precipitation, 10 µL of ammonia (ammonia solution 28–30%) are deposited with the aid of the automated pipetting system to the desired position in the quartz plate, follow by deposition of 5 µL of the desire liquid combination (from the standard plate). The process is repeated for each of the combinations in the standard plate and replicated five times. During the whole time, the quartz plate is heated at 80 °C and after all the depositions are completed, the quartz plate is dried at 80 °C for 1 h.

**Step 3**: The quartz plate is transferred to a furnace in which a heat treatment is carried out at 750 °C for 6 h (heating rate 5 °C min⁻¹—air atmosphere). The quartz plate is let to cool down to room temperature in the furnace.

*Automated X-Ray Diffraction*: XRD experiments were conducted in a STOE Stadi P diffractometer, equipped with a Ga-jet X-ray source using Ga-K$\beta$ radiation (1.207930 Å), with a spot size of ≈200 µm, and an in-house modified XY stage for automated sample measurement. All the X-ray diffractograms were acquired in transmission mode, the samples were carefully scooped from the quartz plate and placed between two polyamide tapes (see Figure S8, Supporting Information for the two polyamide tapes X-ray diffractogram) to an in-house modified holder with 96 positions (designed for automated XRD measurements). For all the samples, a semi-automated Rietveld refinement was made using Xpert Highscore Plus software to calculate the phases present and their respective amounts, lattice parameters, and crystallite size.

*Automated Raman Spectroscopy*: Raman spectra were obtained using a Renishaw Raman microscope with infrared (785 nm) laser in the range of 300–700 cm⁻¹. Three different positions per sample were evaluated and the average of the three spectra was taken. Each spectrum was the result of one accumulation lasting 30 s. The ratio between cumulative intensities of the peak at ≈560–600 cm⁻¹ (originating from the presence of oxygen vacancies) and the peak at ≈460 cm⁻¹ ($F_{2g}$ vibration mode, originating from the vibration of oxygen ions surrounding Ce and Pr cations with +4 oxidation state) is generally used to compare OVC in systems with fluorite structure ($I_{560}/I_{460}$).[84] The Raman peaks are fitted with a Gaussian function using Origin Software. Peaks that cannot be fitted using a single Gaussian are fitted with two Gaussians and the sum

of the two Gaussians are taken as the intensity of the peak (see Section S10, Supporting Information for the Raman fitted spectra).

*Automated Chemical Composition*: A scanning electron microscope (LEO 1530) equipped with an energy dispersive spectroscopy (EDS) detector (Oxford) was used to determine the chemical composition of each sample in the quartz plates. The acceleration voltage was 20 kV, and the working distance 8.5 mm. To avoid charging during the chemical composition acquisition, the quartz plates were sputter coated with a 20 nm gold layer. The AZTEC software (Oxford) was used to map the quartz plates and obtained the chemical composition data (see Table S1, Supporting Information for the chemical composition data, Figures S1 and S2, Supporting Information, for the chemical composition map of the samples in the quartz plate, and Section S10, Supporting Information), the oxygen concentration was not calculated from the EDS spectra due to the substrate effect (made of quartz $SiO_2$), instead O and Si were used for deconvolution and fitting the EDS spectra to obtain the concentration of the cations. For samples 1–15, the mapped area was $60 \times 14$ mm and consist of 106 images. For samples 16–106, the mapped area was $60 \times 70$ mm and consist of 568 images. Each image has an area of $3.27 \times 2.45$ mm, the resolution for data acquisition was $256 \times 192$ pixels (each pixel size ≈12.7 µm).

*Transmission Electron Microscopy*: A Themis-Z (Thermo Fisher) transmission electron microscope (operating at 300 kV) was used to study the phase purity and chemical composition (in scanning-TEM mode) of the specimen. The chemical composition data was collected with a super-X EDX detector. The sample powder was directly dispersed onto a carbon coated copper grid for the TEM studies.

*Automated Ultraviolet–Visible (UV–vis) Spectroscopy*: UV–vis spectra were obtained using a Cary 60 (Agilent) equipped with a remote fiber optic diffuse reflectance accessory (barrelino). The spectra were baseline corrected and run over the range 1100–200 nm with a scan speed of 600 nm min⁻¹, a total of five measurements were made on each sample. The values reported in Figure 5b and in the Supporting Information are the average of all the diffuse reflectance measurements conducted on each sample and can be found in Table S2, Supporting Information. The spot size of the UV source is ≈1 mm diameter. The 100% reflectance baseline was collected using a white PTFE standard. The automated measuring process is shown in Figure 1 and it is driven by a XYZ robot for sample position exchanging. To avoid light interaction with the measurements, the complete device is enclosed within a black box during the measurements period.

The BG value was obtained for each UV–vis spectra by using the analogous Tauc method which is based on the relation between BG ($E_g$) and the Kubelka–Munk (K–M)[87] or reemission function, $F$ ($R∞$).

$$F\left(R_\infty\right) = \frac{K}{S} = \frac{\left(1 - R_\infty\right)^2}{2R_\infty} \tag{2}$$

where $R_\infty = \dfrac{R_{sample}}{R_{standard}}$ is the reflectance of the sample, $K$ and $S$ are the absorption and scattering K–M coefficients, respectively. The analogous Tauc method can be expressed by the relation

$$\left(F\left(R_\infty\right) h\nu\right)^{\frac{1}{\gamma}} = C\left(h\nu - E_g\right) \tag{3}$$

where $h$ is the Planck constant, $\nu$ is the photon's frequency, $E_g$ is the band gap energy, and $C$ is a constant. The $\gamma$ factor depends on the nature of the electron transition and is equal to 1/2 or 2 for the direct and indirect transition band gaps, respectively.[87] The BG value is obtained at the intersection of the linear region of the analogous Tauc plot, $\left(F\left(R_\infty\right)h\nu\right)^{\frac{1}{\gamma}}$ vs $h\nu$, in the photon energy axis ($h\nu$). The transformed data and BG value extraction are displayed in Section S10, Supporting Information for all the samples.

*Machine Learning*: The machine learning model for binary classification of XRD diffractograms was trained on a synthetic dataset with 5000 samples which was constructed based on three reference XRD diffractograms of pure Fm-3m, Ia-3, and P63/m. The

diffractograms were shifted and scaled in *x*- and *y*-direction and added to Gaussian noise and randomized smooth background signals (third order polynomials). In 50% of the cases, random additional Gaussian peaks or additional reference diffractograms were added to generate artificial XRD diffractograms of non-pure phases. Using this procedure, we generated a synthetic dataset of 5000 diffractograms, which we used to train a convolutional neural network (CNN). A discretized form of the XRD intensities were used as an input vector, followed by three 1D convolutional layers with ten kernels of size 5 each, ReLU activations, same padding, followed by 5% dropout and max-pooling with size 2 and stride 2, ending with a densely connected ReLU layer with 150 neurons, L1 and L2 regularization (regularization parameter 0.001) 5% dropout and finally a simple neuron with a Sigmoid activation function for binary classification. The Adam optimizer and a binary-crossentropy loss function were used for training, with a learning rate starting with $10^{-2}$ for 100 epochs, followed by an exponential learning rate decay to $10^{-4}$ for additional 100 epochs. The training curve is shown in Figure S5, Supporting Information. SHapley Additive exPlanations (SHAP) analysis of the trained neural network was performed to obtain intuitive interpretations of the machine learning model.

The test set accuracy on the synthetic data is ≈94%, while on the real experimental data which was not used for training, we obtain an accuracy of 86%, that is, 91 of 106 samples were classified correctly (see Supporting Information for further discussion). All wrong classifications were pure phases which the CNN model predicted as mixed. All CNN predictions are associated to a classification (un)certainty, which can be used in a semi-autonomous system to decide if manual post-processing and analysis is required. Furthermore, we used SHAP analysis to generate intuitive insights into the predictions of the neural network.[88]

A second machine learning model (logistic regression) was trained on the 106 experimentally measured data points with only the HEO compositions plus logical "and" combinations of the compositions as an input. Analysis of the logistic regression coefficients shows the importance and influence of the input features with respect to the prediction.

## Supporting Information

Supporting Information is available from the Wiley Online Library or from the author.

## Acknowledgements

## Conflict of Interest

The authors declare no conflict of interest.

## Data Availability Statement

The data that support the findings of this study are available within the paper; Supplementary Information; and text files containing all the X-ray diffractograms, Raman spectra, and UV–vis spectra. Additional data are available from the corresponding author upon reasonable request. The machine learning code and data are available on https://github.com/aimat-lab/ML4HEOs.

[1] R. Potyrailo, K. Rajan, K. Stoewe, I. Takeuchi, B. Chisholm, H. Lam, *ACS Comb. Sci.* **2011**, *13*, 579.

[2] T. Gebhardt, D. Music, T. Takahashi, J. M. Schneider, *Thin Solid Films* **2012**, *520*, 5491.

[3] D. P. Tabor, L. M. Roch, S. K. Saikin, C. Kreisbeck, D. Sheberla, J. H. Montoya, S. Dwaraknath, M. Aykol, C. Ortiz, H. Tribukait, C. Amador-Bedolla, C. J. Brabec, B. Maruyama, K. A. Persson, A. Aspuru-Guzik, *Nat. Rev. Mater.* **2018**, *3*, 5.

[4] J. W. Yeh, S. K. Chen, S. J. Lin, J. Y. Gan, T. S. Chin, T. T. Shun, C. H. Tsau, S. Y. Chang, *Adv. Eng. Mater.* **2004**, *6*, 299.

[5] B. Cantor, I. T. H. Chang, P. Knight, A. J. B. Vincent, *Mater. Sci. Eng. A* **2004**, *375–377*, 213.

[6] J. W. Yeh, S. J. Lin, *J. Mater. Res.* **2018**, *33*, 3129.

[7] E. Castle, T. Csanádi, S. Grasso, J. Dusza, M. Reece, *Sci. Rep.* **2018**, *8*, 8609.

[8] C. M. Rost, E. Sachet, T. Borman, A. Moballegh, E. C. Dickey, D. Hou, J. L. Jones, S. Curtarolo, J. P. Maria, *Nat. Commun.* **2015**, *6*, 8485.

[9] T. Jin, X. Sang, R. R. Unocic, R. T. Kinch, X. Liu, J. Hu, H. Liu, S. Dai, *Adv. Mater.* **2018**, *30*, 1707512.

[10] Q. Wang, A. Sarkar, Z. Li, Y. Lu, L. Velasco, S. S. Bhattacharya, T. Brezesinski, H. Hahn, B. Breitung, *Electrochem. Commun.* **2019**, *100*, 121.

[11] X. Yan, Y. Zhang, *Scr. Mater.* **2020**, *187*, 188.

[12] F. Zhang, C. Zhang, S. L. Chen, J. Zhu, W. S. Cao, U. R. Kattner, *CALPHAD: Comput. Coupling Phase Diagrams Thermochem.* **2014**, *45*, 1.

[13] Y. Zhang, Y. J. Zhou, J. P. Lin, G. L. Chen, P. K. Liaw, *Adv. Eng. Mater.* **2008**, *10*, 534.

[14] B. Burger, P. M. Maffettone, V. V. Gusev, C. M. Aitchison, Y. Bai, X. Wang, X. Li, B. M. Alston, B. Li, R. Clowes, N. Rankin, B. Harris, R. S. Sprick, A. I. Cooper, *Nature* **2020**, *583*, 237.

[15] Z. Li, M. A. Najeeb, L. Alves, A. Z. Sherman, V. Shekar, P. C. Parrilla, I. M. Pendleton, W. Wang, P. W. Nega, M. Zeller, J. Schrier, A. J. Norquist, E. M. Chan, *Chem. Mater.* **2020**, *32*, 5650.

[16] A. Ludwig, *npj Comput. Mater.* **2019**, *5*, 7.

[17] C. Wen, Y. Zhang, C. Wang, D. Xue, Y. Bai, S. Antonov, L. Dai, T. Lookman, Y. Su, *Acta Mater.* **2019**, *170*, 109.

[18] R. D. King, J. Rowland, S. G. Oliver, M. Young, W. Aubrey, E. Byrne, M. Liakata, M. Markham, P. Pir, L. N. Soldatova, A. Sparkes, K. E. Whelan, A. Clare, *Science* **2009**, *324*, 85.

[19] S. Langner, F. Häse, J. D. Perea, T. Stubhan, J. Hauch, L. M. Roch, T. Heumueller, A. Aspuru-Guzik, C. J. Brabec, *Adv. Mater.* **2020**, *32*, 1907801.

[20] P. Nikolaev, D. Hooper, F. Webber, R. Rao, K. Decker, M. Krein, J. Poleski, R. Barto, B. Maruyama, *npj Comput. Mater.* **2016**, *2*, 16031.

[21] S. Sun, A. Tiihonen, F. Oviedo, Z. Liu, J. Thapa, Y. Zhao, N. T. P. Hartono, A. Goyal, T. Heumueller, C. Batali, A. Encinas, J. J. Yoo, R. Li, Z. Ren, I. M. Peters, C. J. Brabec, M. G. Bawendi, V. Stevanovic, J. Fisher, T. Buonassisi, *Matter* **2021**, *4*, 1305.

**ADVANCED
SCIENCE NEWS**

www.advancedsciencenews.com

**ADVANCED
MATERIALS**

www.advmat.de

[22] M. Saliba, *Adv. Energy Mater.* **2019**, *9*, 1803754.

[23] J. Kirman, A. Johnston, D. A. Kuntz, M. Askerka, Y. Gao, P. Todorović, D. Ma, G. G. Privé, E. H. Sargent, *Matter* **2020**, *2*, 938.

[24] K. Higgins, S. M. Valleti, M. Ziatdinov, S. V. Kalinin, M. Ahmadi, *ACS Energy Lett.* **2020**, *5*, 3426.

[25] A. M. Cassell, S. Verma, L. Delzeit, M. Meyyappan, J. Han, *Langmuir* **2001**, *17*, 260.

[26] S. Noda, Y. Tsuji, Y. Murakami, S. Maruyama, *Appl. Phys. Lett.* **2005**, *86*, 173106.

[27] C. R. Oliver, W. Westrick, J. Koehler, A. Brieland-Shoultz, I. Anagnostopoulos-Politis, T. Cruz-Gonzalez, A. J. Hart, *Rev. Sci. Instrum.* **2013**, *84*, 115105.

[28] P. Nikolaev, D. Hooper, N. Perea-López, M. Terrones, B. Maruyama, *ACS Nano* **2014**, *8*, 10214.

[29] G. Kumar, H. Bossert, D. McDonald, A. Chatzidimitriou, M. A. Ardagh, Y. Pang, C. S. Lee, M. Tsapatsis, O. A. Abdelrahman, P. J. Dauenhauer, *Matter* **2020**, *3*, 805.

[30] R. Gómez-Bombarelli, J. Aguilera-Iparraguirre, T. D. Hirzel, D. Duvenaud, D. Maclaurin, M. A. Blood-Forsythe, H. S. Chae, M. Einzinger, D. G. Ha, T. Wu, G. Markopoulos, S. Jeon, H. Kang, H. Miyazaki, M. Numata, S. Kim, W. Huang, S. I. Hong, M. Baldo, R. P. Adams, A. Aspuru-Guzik, *Nat. Mater.* **2016**, *15*, 1120.

[31] A. Saeki, K. Kranthiraja, *Jpn. J. Appl. Phys.* **2020**, *59*, SD0801.

[32] J. C. Grunlan, A. R. Mehrabi, A. T. Chavira, A. B. Nugent, D. L. Saunders, *J. Comb. Chem.* **2003**, *5*, 362.

[33] C. Neuber, M. Bäte, M. Thelakkat, H. W. Schmidt, H. Hänsel, H. Zettl, G. Krausch, *Rev. Sci. Instrum.* **2007**, *78*, 072216.

[34] A. Rar, J. J. Frafjord, J. D. Fowlkes, E. D. Specht, P. D. Rack, M. L. Santella, H. Bei, E. P. George, G. M. Pharr, *Meas. Sci. Technol.* **2005**, *16*, 46.

[35] Y. Han, B. Matthews, D. Roberts, K. R. Talley, S. R. Bauers, C. Perkins, Q. Zhang, A. Zakutayev, *ACS Comb. Sci.* **2018**, *20*, 436.

[36] E. D. Specht, A. Rar, G. M. Pharr, E. P. George, P. Zschack, H. Hong, J. Ilavsky, *J. Mater. Res.* **2003**, *18*, 2522.

[37] X. D. Xiang, X. Sun, G. Briceño, Y. Lou, K. A. Wang, H. Chang, W. G. Wallace-Freedman, S. W. Chen, P. G. Schultz, *Science* **1995**, *268*, 1738.

[38] J. J. Hanak, *J. Mater. Sci.* **1970**, *5*, 964.

[39] K. Kennedy, T. Stefansky, G. Davy, V. F. Zackay, E. R. Parker, *J. Appl. Phys.* **1965**, *36*, 3808.

[40] G. Briceño, H. Chang, X. Sun, P. G. Schultz, X. D. Xiang, *Science* **1995**, *270*, 273.

[41] E. M. Chan, C. Xu, A. W. Mao, G. Han, J. S. Owen, B. E. Cohen, D. J. Milliron, *Nano Lett.* **2010**, *10*, 1874.

[42] N. M. Al Hasan, H. Hou, T. Gao, J. Counsell, S. Sarker, S. Thienhaus, E. Walton, P. Decker, A. Mehta, A. Ludwig, I. Takeuchi, *ACS Comb. Sci.* **2020**, *22*, 641.

[43] N. M. Al Hasan, H. Hou, S. Sarker, S. Thienhaus, A. Mehta, A. Ludwig, I. Takeuchi, *Engineering* **2020**, *6*, 637.

[44] H. Dobbelstein, E. L. Gurevich, E. P. George, A. Ostendorf, G. Laplanche, *Addit. Manuf.* **2019**, *25*, 252.

[45] S. Kumari, J. R. C. Junqueira, W. Schuhmann, A. Ludwig, *ACS Comb. Sci.* **2020**, *22*, 844.

[46] L. Zhao, Y. Zhou, H. Wang, X. Chen, L. Yang, L. Zhang, L. Jiang, Y. Jia, X. Chen, H. Wang, *Metall. Mater. Trans. A Phys. Metall. Mater. Sci.* **2021**, *52*, 1159.

[47] S. Guerin, B. E. Hayden, *J. Comb. Chem.* **2006**, *8*, 66.

[48] M. Matsubara, A. Suzumura, N. Ohba, R. Asahi, *Commun. Mater.* **2020**, *1*, 5.

[49] A. Ludwig, R. Zarnetta, S. Hamann, A. Savan, S. Thienhaus, *Zeitschrift fuer Met. Res. Adv. Tech.* **2008**, *99*, 1144.

[50] R. Mertens, Z. Sun, D. Music, J. M. Schneider, *Adv. Eng. Mater.* **2004**, *6*, 903.

[51] H. Knoll, S. Ocylok, A. Weisheit, H. Springer, E. Jägle, D. Raabe, *Steel Res. Int.* **2017**, *88*, 1600416.

[52] J. C. Zhao, X. Zheng, D. G. Cahill, *Mater. Today* **2005**, *8*, 28.

[53] H. Springer, D. Raabe, *Acta Mater.* **2012**, *60*, 4950.

[54] P. Wilson, R. Field, M. Kaufman, *Intermetallics* **2016**, *75*, 15.

[55] Z. Li, A. Ludwig, A. Savan, H. Springer, D. Raabe, *J. Mater. Res.* **2018**, *33*, 3156.

[56] K. G. Pradeep, C. C. Tasan, M. J. Yao, Y. Deng, H. Springer, D. Raabe, *Mater. Sci. Eng. A* **2015**, *648*, 183.

[57] T. Borkar, V. Chaudhary, B. Gwalani, D. Choudhuri, C. V. Mikler, V. Soni, T. Alam, R. V. Ramanujan, R. Banerjee, *Adv. Eng. Mater.* **2017**, *19*, 1700048.

[58] T. Borkar, B. Gwalani, D. Choudhuri, C. V. Mikler, C. J. Yannetta, X. Chen, R. V. Ramanujan, M. J. Styles, M. A. Gibson, R. Banerjee, *Acta Mater.* **2016**, *116*, 63.

[59] Y. Xu, Y. Bu, J. Liu, H. Wang, *Scr. Mater.* **2019**, *160*, 44.

[60] F. Oviedo, Z. Ren, S. Sun, C. Settens, Z. Liu, N. T. P. Hartono, S. Ramasamy, B. L. DeCost, S. I. P. Tian, G. Romano, A. Gilad Kusne, T. Buonassisi, *npj Comput. Mater.* **2019**, *5*, 60.

[61] Y. Suzuki, H. Hino, T. Hawai, K. Saito, M. Kotsugi, K. Ono, *Sci. Rep.* **2020**, *10*, 21790.

[62] J. W. Lee, W. B. Park, J. H. Lee, S. P. Singh, K. S. Sohn, *Nat. Commun.* **2020**, *11*, 86.

[63] H. Wang, Y. Xie, D. Li, H. Deng, Y. Zhao, M. Xin, J. Lin, *J. Chem. Inf. Model.* **2020**, *60*, 2004.

[64] A. Ziletti, D. Kumar, M. Scheffler, L. M. Ghiringhelli, *Nat. Commun.* **2018**, *9*, 2775.

[65] K. Utimula, R. Hunkao, M. Yano, H. Kimoto, K. Hongo, S. Kawaguchi, S. Suwanna, R. Maezono, *Adv. Theory Simul.* **2020**, *3*, 2000039.

[66] D. B. Miracle, O. N. Senkov, *Acta Mater.* **2017**, *122*, 448.

[67] J. E. Saal, S. Kirklin, M. Aykol, B. Meredig, C. Wolverton, *JOM* **2013**, *65*, 1501.

[68] S. Kirklin, J. E. Saal, B. Meredig, A. Thompson, J. W. Doak, M. Aykol, S. Rühl, C. Wolverton, *npj Comput. Mater.* **2015**, *1*, 15010.

[69] C. Zhang, F. Zhang, S. Chen, W. Cao, *JOM* **2012**, *64*, 839.

[70] O. N. Senkov, S. V. Senkova, C. Woodward, D. B. Miracle, *Acta Mater.* **2013**, *61*, 1545.

[71] A. Sarkar, C. Loho, L. Velasco, T. Thomas, S. S. Bhattacharya, H. Hahn, R. R. Djenadic, *Dalt. Trans.* **2017**, *46*, 12167.

[72] H. Xu, Z. Zhang, J. Liu, C. L. Do-Thanh, H. Chen, S. Xu, Q. Lin, Y. Jiao, J. Wang, Y. Wang, Y. Chen, S. Dai, *Nat. Commun.* **2020**, *11*, 3908.

[73] A. Sarkar, R. Djenadic, N. J. Usharani, K. P. Sanghvi, V. S. K. Chakravadhanula, A. S. Gandhi, H. Hahn, S. S. Bhattacharya, *J. Eur. Ceram. Soc.* **2017**, *37*, 747.

[74] M. Biesuz, L. Spiridigliozzi, G. Dell'Agli, M. Bortolotti, V. M. Sglavo, *J. Mater. Sci.* **2018**, *53*, 8074.

[75] H. Fleischer, D. Baumann, S. Joshi, X. Chu, T. Roddelkopf, M. Klos, K. Thurow, *Energies* **2018**, *11*, 2567.

[76] B. P. MacLeod, F. G. L. Parlane, T. D. Morrissey, F. Häse, L. M. Roch, K. E. Dettelbach, R. Moreira, L. P. E. Yunker, M. B. Rooney, J. R. Deeth, V. Lai, G. J. Ng, H. Situ, R. H. Zhang, M. S. Elliott, T. H. Haley, D. J. Dvorak, A. Aspuru-Guzik, J. E. Hein, C. P. Berlinguette, *Sci. Adv.* **2020**, *6*, eaaz8867.

[77] P. S. Gromski, J. M. Granda, L. Cronin, *Trends Chem.* **2020**, *2*, 4.

[78] S. Sun, N. T. P. Hartono, Z. D. Ren, F. Oviedo, A. M. Buscemi, M. Layurova, D. X. Chen, T. Ogunfunmi, J. Thapa, S. Ramasamy, C. Settens, B. L. DeCost, A. G. Kusne, Z. Liu, S. I. P. Tian, I. M. Peters, J. P. Correa-Baena, T. Buonassisi, *Joule* **2019**, *3*, 1437.

[79] G. Y. Adachi, N. Imanaka, *Chem. Rev.* **1998**, *98*, 1479.

[80] R. Schmitt, A. Nenning, O. Kraynis, R. Korobko, A. I. Frenkel, I. Lubomirsky, S. M. Haile, J. L. M. Rupp, *Chem. Soc. Rev.* **2020**, *49*, 554.

[81] C. Mao, Y. Zhao, X. Qiu, J. Zhu, C. Burda, *Phys. Chem. Chem. Phys.* **2008**, *10*, 5633.

**ADVANCED
SCIENCE NEWS**

www.advancedsciencenews.com

**ADVANCED
MATERIALS**

www.advmat.de

[82] G. R. Bamwenda, H. Arakawa, *J. Mol. Catal. A: Chem.* **2000**, *161*, 105.

[83] A. Corma, P. Atienzar, H. García, J. Y. Chane-Ching, *Nat. Mater.* **2004**, *3*, 394.

[84] Z. Y. Pu, J. Q. Lu, M. F. Luo, Y. L. Xie, *J. Phys. Chem. C* **2007**, *111*, 18695.

[85] J. J. Kim, S. R. Bishop, D. Chen, H. L. Tuller, *Chem. Mater.* **2017**, *29*, 1999.

[86] A. Sarkar, B. Eggert, L. Velasco, X. Mu, J. Lill, K. Ollefs, S. S. Bhattacharya, H. Wende, R. Kruk, R. A. Brand, H. Hahn, *APL Mater.* **2020**, *8*, 051111.

[87] A. Escobedo-Morales, I. I. Ruiz-López, M. de, L. Ruiz-Peralta, L. Tepech-Carrillo, M. Sánchez-Cantú, J. E. Moreno-Orea, *Heliyon* **2019**, *5*, e01505.

[88] S. M. Lundberg, S. I. Lee, *Adv. Neural Inf. Process. Syst.* **2017**, *2017*, 4766.

2102301  (11 of 11)